SCIENTIFIC REP⚙RTS

OPEN

Erosion potential of the Yangtze Delta under sediment starvation and climate change

H. F. Yang[1,2], S. L. Yang[1], K. H. Xu[2,3], H. Wu[1], B. W. Shi[2,4], Q. Zhu[1,5], W. X. Zhang[1] & Z. Yang[6]

Deltas are widely threatened by sediment starvation and climate change. Erosion potential is an important indicator of delta vulnerability. Here, we investigate the erosion potential of the Yangtze Delta. We found that over the past half century the Yangtze's sediment discharge has decreased by 80% due to the construction of >50,000 dams and soil conservation, whereas the wind speed and wave height in the delta region have increased by 5–7%, and the sea level has risen at a rate of 3 mm/ yr. According to hydrodynamic measurements and analyses of seabed sediments, the period when bed shear stress due to combined current-wave action under normal weather conditions exceeds the critical bed shear stress for erosion (τ_{cr}) accounts for 63% of the total observed period on average and can reach 100% during peak storms. This explains why net erosion has occurred in some areas of the subaqueous delta. We also found that the increase with depth of τ_{cr} is very gradual in the uppermost several metres of the depositional sequence. We therefore expect that the Yangtze subaqueous delta will experience continuous erosion under sediment starvation and climate change in the next decades of this century or even a few centuries.

Deltas, which are depositional systems of riverine sediments, are densely populated socio-economic centres. However, many deltas are now threatened by human-induced sediment starvation and climate change[1–3]. In extreme examples, such as the Nile and Colorado deltas, sediment discharges have decreased to almost zero. In the Mississippi, Yellow and many other rivers, the sediment discharges to the sea have also declined by 60–90% in recent decades[4–6]. This sediment starvation in deltas has mainly been caused by river damming, although water diversion and soil conservation within watersheds also play roles[7–9]. Additionally, global warming has been an important scientific and environmental issue[10, 11]. Under these conditions, some studies have revealed that sea surface wind speeds and wind wave heights have increased[12, 13]. Deltas' response to sediment starvation and hydrodynamic increase depend on the contrast between the marine hydrodynamics and seabed sediment properties and can differ between rivers. Previous studies on delta erosion have mainly focused on coastline retreat[6, 14–18]. Less is known about the response of broad subaqueous deltas to sediment starvation due to a lack of bathymetric and stratigraphic data. Detecting erosion or determining the erosion potential in delta coasts is very important to both ecology and management because many oil pipelines and optic cables are shallowly buried beneath the seabed of deltaic coasts. Thus, an urgent need exists to investigate the erodibility and predict the erosion potential of subaqueous deltas, particularly for large rivers.

The Yangtze River is one of the world's largest rivers in terms of water discharge (900 km³/yr) and sediment load (500 Mt/yr before decline; Mt: million tons) and is the largest in terms of its watershed population (450 million)[6, 19]. In recent decades, approximately 50,000 dams have been constructed within the Yangtze watersheds. Among them, the world's largest hydropower project, the Three Gorges Reservoir (TGR)[20], began its operation on the main stem of the Yangtze River in 2003, and a series of cascade dams, whose cumulative reservoir capacity exceeds that of the TGR (Fig. 1a), began their operation in the largest and previously undammed Jinshajiang

[1]State Key Laboratory of Estuarine and Coastal Research, East China Normal University, Shanghai, 200062, China. [2]Department of Oceanography and Coastal Sciences, Louisiana State University, Baton Rouge, LA, 70803, USA. [3]Coastal Studies Institute, Louisiana State University, Baton Rouge, LA, 70803, USA. [4]Ministry of Education Key Laboratory for Coast and Island Development, Nanjing University, Nanjing, 210093, China. [5]Department of Hydraulic Engineering, Faculty Civil Engineering and Geosciences, Delft University of Technology, P.O. Box 5048, 2600 GA, Delft, The Netherlands. [6]College of Marine Geosciences, Ocean University of China, 238 Songling Rd., Qingdao, 266100, China. Correspondence and requests for materials should be addressed to S.L.Y. (email: slyang@sklec.ecnu. edu.cn)
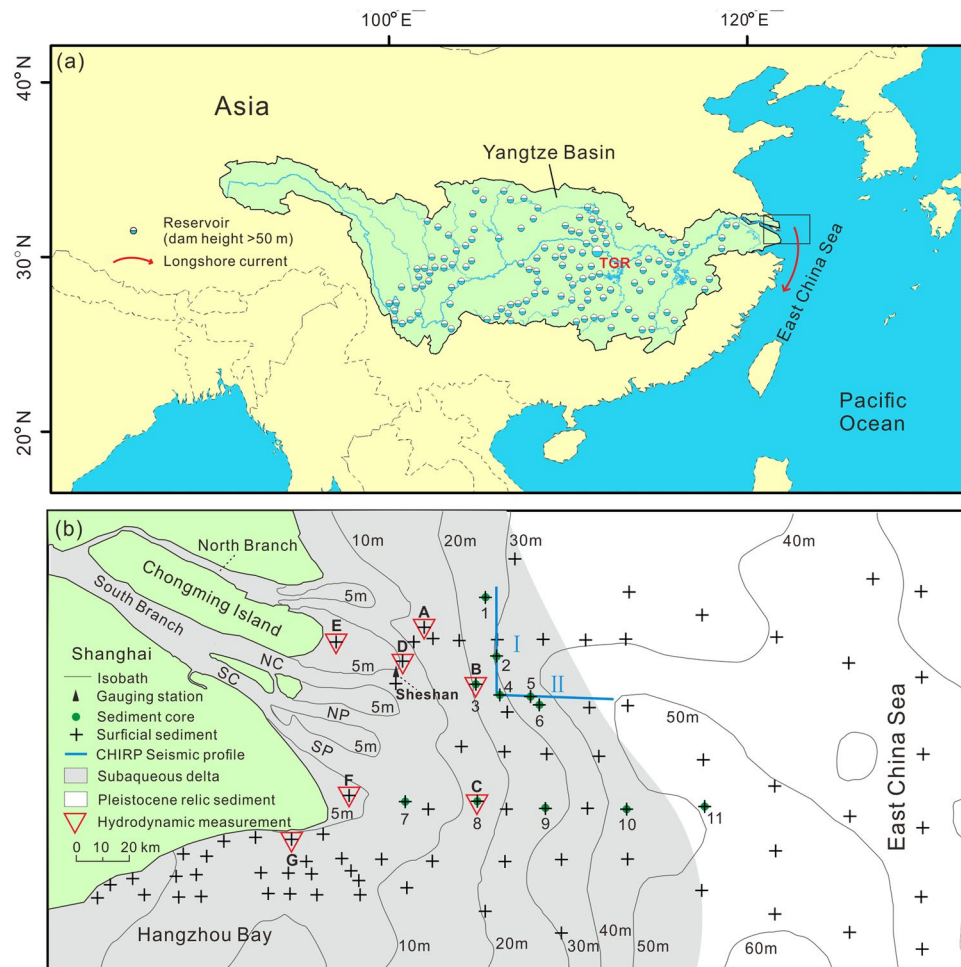
1

Figure 1. Location and background of the Yangtze River Delta (**a**) and the sediment sampling and hydrodynamic observation sites (**b**). Main reservoirs with dam height >50 m in the Yangtze basin are shown in Fig. 1a. In Fig. 1b, the area in grey represents the subaqueous delta, and the area in white represents the Pleistocene relic sand. NC: North Channel, SC: South Channel, NP: North Passage, and SP: South Passage. The figures were created using ArcGIS 10.1 (www.esri.com/software/arcgis) and CorelDRAW Graphics Suite X6 (http://www.coreldraw.com/en/product/graphic-design-software).

sub-basin in 2012–2015. In addition, large-scale soil conservation has been conducted[9]. Thus, the Yangtze's sediment discharge to the sea has decreased by nearly 80% (<120 Mt/yr in 2013–2015). Yang et al.[21] reported erosion in an 1800-km² area of this delta between 2004 and 2007. However, a later study found that the accumulation in this area had rebounded[22]. Recently, new evidences of erosion in the Yangtze subaqueous delta have been found, either within areas that were not previously studied or due to updated data for the previously studied areas[23–25]. The above controversy reflects the complexity of a delta's response to sediment starvation. The entire area of the Yangtze subaqueous delta exceeds 10,000 km². For most of this area, bathymetric data in high spatial and temporal resolutions are unavailable for ascertaining the morphological response to sediment starvation. Thus, we must develop a hydrodynamic-sedimentary approach to examine the morphological trends of the broad delta.

During our study, the interannual variations of tidal ranges were relatively small with the difference between the minimum and maximum <6%[25]. Our observations were mainly conducted in July and August under normal weather conditions, when tidal ranges were close to mean annual value with the difference <5%[26]. Compared to the monthly and interannual variations of tidal ranges, the difference between spring and neap tides are quite large[27]. Therefore, observations lasting for more than 2 tidal cycles during both spring and neap tides were conducted to study the average condition of hydrodynamics in the Yangtze Delta. In this study, we aim to investigate the hydrodynamic mechanisms of delta erosion under sediment starvation and predict the future erosion potential of the Yangtze subaqueous delta. Our objectives are to (1) determine the bed shear stress due to the combined current-wave action (τ_{cw}), (2) determine the critical shear stress for the erosion of sediment (τ_{cr}), (3) compare the values of τ_{cw} with those of τ_{cr} and quantify the sediment erodibility, (4) ascertain the thickness of sediment that is erodible under sediment starvation and combined current-wave action, (5) discuss whether this subaqueous delta will experience extensive erosion and how long this erosion could continue.
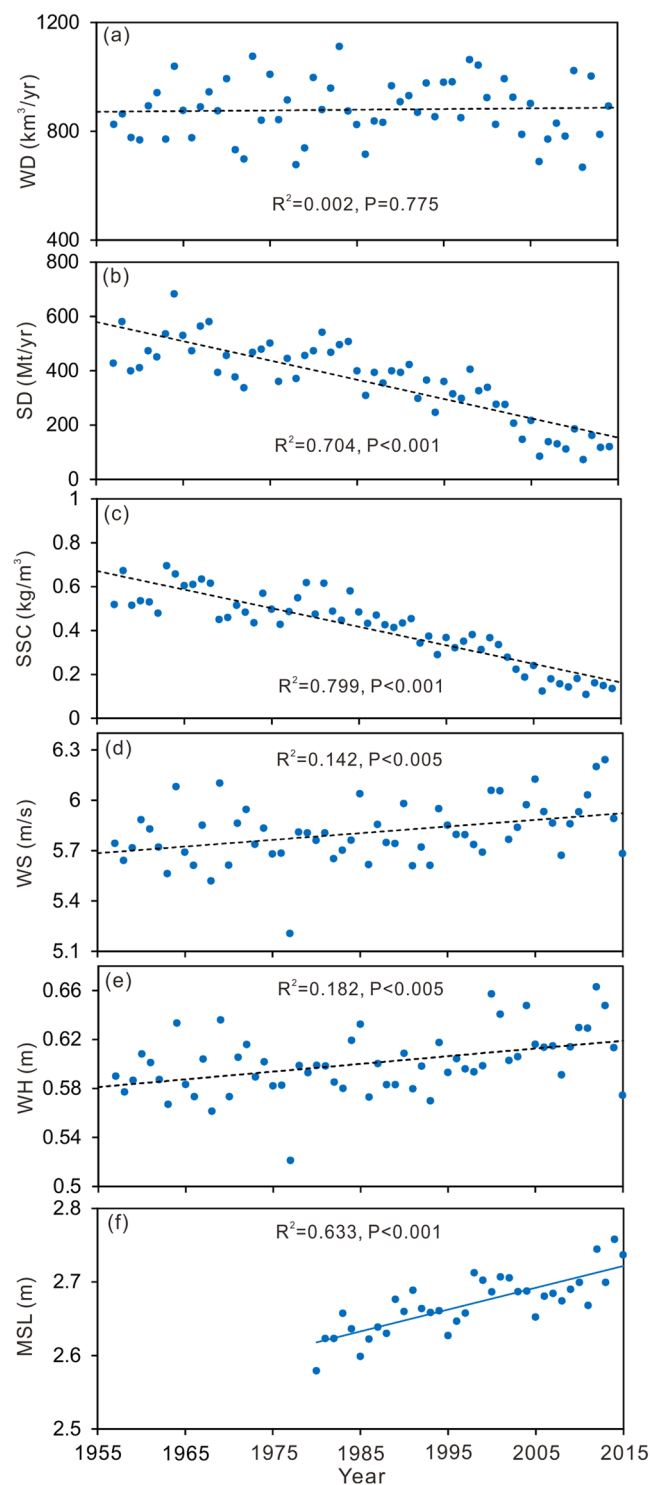
Figure 2. Temporal changes of the annual water discharge (**a**), sediment discharges (**b**) and suspended sediment concentration (**c**) in the Yangtze River, annual average wind speed (**d**) and significant wave height (**e**) at Sheshan station, and annual mean sea level (above the Astronomic Lowest Tide) in the Northern East China Sea (**f**). The location of Sheshan station was noted in Fig. 1b. WD: water discharge, SD: sediment discharge, SSC: suspended sediment concentration, WS: wind speed, WH: wave height and MSL: mean sea level.

Results

Temporal variations in environmental drivers.   No evident trend ($P \gg 0.050$) in annual water discharge from the Yangtze River was found, which has remained at a steady level of approximately 900 km³/yr since the mid 1950s (Fig. 2a). However, the riverine sediment discharge decreased very significantly ($P < 0.001$) from

			Site A	Site B	Site C	Site D	Site E	Site F	Site G
τ_{cw} (N/m²)	Normal winds	Neap tide	0.08	0.23	0.18	0.11	0.16	0.15	0.38
		Spring tide	0.24	0.32	0.31	0.67	0.20	0.41	0.57
		Average	0.16	0.28	0.25	0.39	0.18	0.28	0.48
	Peak storm	Spring tide	ND	ND	ND	ND	ND	ND	2.56
τ_{cr} (N/m²)	Surficial sediment		0.11	0.09	0.09	0.14	0.18	0.23	0.16
	Core sediment (average)		ND	0.10	0.09	ND	ND	ND	ND
Period of $\tau_{cw} > \tau_{cr}$ in observation (%)	Normal winds	Neap tide	31	66	73	23	41	21	79
		Spring tide	82	81	91	78	58	78	81
		Average	57	74	82	51	50	50	80
	Peak storm	Spring tide	ND	ND	ND	ND	ND	ND	100

Table 1. Tide-averaged τ_{cw} and τ_{cr} and percent of period when $\tau_{cw} > \tau_{cr}$ in observations at the seven sites. ND: No data are available. Each measurement was continuously conducted for 26 hours.

approximately 500 Mt/yr in the 1950s to only approximately 130 Mt/yr in the 2010s (Fig. 2b). Thus, the riverine suspended sediment concentration exhibited a temporal trend (P < 0.001) similar to the riverine sediment discharge (Fig. 2c). In the meantime, slight increasing trends in both the annual wind speed (P < 0.005) and significant wave height (P < 0.005) were found during the past approximately 60 years (Fig. 2d,e). The annual average wind speed increased from 5.70 m/s in the 1950s to 6.00 m/s in the 2010s, and the annual average significant wave height increased from 0.58 m in the 1950s to 0.63 m in the 2010s. The mean sea level in the northern East China Sea showed a significant rising trend (P < 0.001), and the average rate of sea level rise was approximately 3 mm/yr during the past approximately 35 years (Fig. 2f).

Variability of τ_{cw}. τ_{cw} was highly variable in time and space. Under normal wind conditions, the τ_{cw} values ranged from 0.08 to 0.67 N/m² and were 0.29 N/m² on average. The lowest τ_{cw} values were usually found in slack waters at low and high tides, and the peak τ_{cw} values tended to occur at mean tidal level, when the current velocity was the greatest. The τ_{cw} during spring tides was 2.1 times greater than that during neap tides on average. The time-averaged τ_{cw} values at A, B, C, D, E, F and G were 0.16, 0.28, 0.25, 0.39, 0.18, 0.28 and 0.48 N/m², respectively (Table 1). During a peak storm event (spring tide), the τ_{cw} values at a shallow site (G) ranged from 0.73 to 4.79 N/m² and were 2.56 N/m² on average, which was 4.5 times greater than that under normal wind conditions (spring tide) (Fig. 3, Supplementary Fig. S1 and Table 1).

The τ_{cw} in the Yangtze's subaqueous delta was generally dominated by tidal action. The wave-induced shear stress at the depth of 20 m decreased by >98% compared to that at the depth of 2 m. More than 95% of the τ_{cw} at the observation sites with water depths that exceeded 10 m could be attributed to tidal action. However, the τ_{cw} on the intertidal flats was dominated by wave action during storm events and very shallow water phases of tidal cycles (water depth < 0.5 m) under normal weather conditions. The mean wind speed at site G increased from 6.3 m/s under normal weather conditions to 11.5 m/s during peak storms (Table 2), and in response, the mean significant wave height increased from 0.22 m to 0.65 m. The mean τ_w was only 0.05 N/m² under normal weather conditions, while it increased to 0.85 N/m² during peak storms (Supplementary Fig. S2). The maximum value for wave-induced shear stress even reached 1.62 N/m², which represented an increase of more than one order of magnitude compared to that under normal weather conditions. Meanwhile, the striking changes were also detected during pre-peak storm and post-peak storm periods compared to that under normal weather conditions at site G. The mean wind speeds were 9.0 m/s during pre-storm period and 7.8 m/s during post-peak storm period, and the mean significant wave heights were 0.29 m and 0.30 m accordingly. Therefore, the mean τ_w were 0.23 N/m² during pre-peak storm period and 0.24 N/m² during post-peak storm period.

Based on the historical data at Sheshan station, the hourly average of wind speed in the Yangtze Delta ranged from 0.01 to 24.1 m/s during the past 60 years, and the multi-year average was 5.8 m/s. Meanwhile, the hourly average of significant wave height ranged from 0.01 to 3.1 m, and the multi-year average was 0.6 m. During our observation of peak storms, the mean wind speed was 11.5 m/s and the mean significant wave height was 1.4 m at Sheshan station, which were both higher than 98% of the records (Supplementary Fig. S3). Considering that storm events (wind speed > 10.8 m/s, grade of storms: http://www.sac.gov.cn/) accounted for 4% of the whole time (Supplementary Fig. S3a), our observation of peak storms was just at a moderate level among all the storms. During the most powerful storms of the past 60 years, the τ_w on the intertidal flats could be more than the double of our measured values in this observation.

Spatial distributions of sediment grain size, water content and τ_{cr}. The surficial sediment of the Yangtze Delta is overall small in grain size and high in water content. The median size (D_{50}) of the surficial sediments in the study area ranged from 5 to 294 μm and was 82 μm on average. In the Yangtze subaqueous delta, the D_{50} values averaged 37 μm, which is significantly lower than the average D_{50} of the Pleistocene relic sediments (Fig. 1b) in the deeper East China Sea (198 μm). Differences in D_{50} were also found within the Yangtze subaqueous delta. The D_{50} values averaged 244 μm in the delta front off the North Branch and averaged only 18 μm in the areas offshore of the South Branch's outlets (Fig. 4a). The water content of the surficial sediments ranged from 25% to 106% and was 46% on average. The water content in the Pleistocene relic sands averaged 30%, whereas
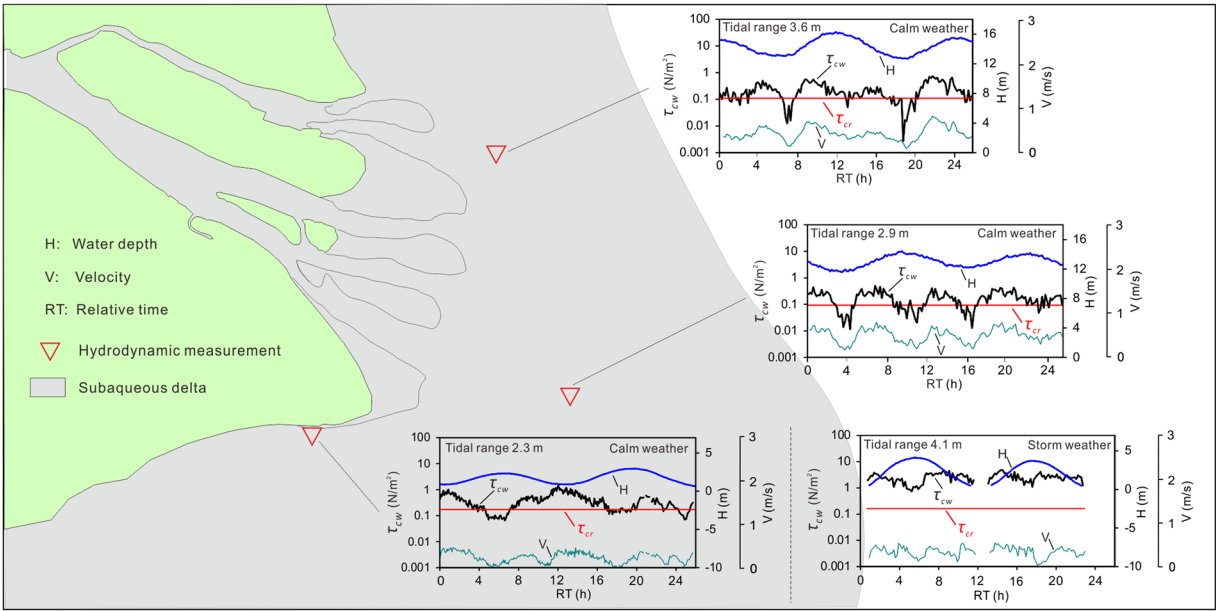
Figure 3. Four examples showing intratidal variations in the water depth, near-bed velocity and combined current-wave shear stress (τ_{cw}) compared to the critical bed shear stress (τ_{cr}) at the observation stations. A complete exhibition of all the observations was in the attached Supplementary Fig. S1. The figures were created using ArcGIS 10.1 (www.esri.com/software/arcgis) and CorelDRAW Graphics Suite X6 (http://www.coreldraw.com/en/product/graphic-design-software).

	Site A	Site B	Site C	Site D	Site E	Site F	Site G
Mean water depth (m)	14	21	13	7.5	0.72	1.7	2.2
Mean wind speed (m/s)*	6.2	6.0	5.9	4.4	5.9	4.9	6.3/11.5
Wind strength	Normal	Normal	Normal	Normal	Normal	Normal	Normal/stormy
Tide type	Neap, Spring	Neap, Spring	Neap, Spring	Neap, Spring	Neap, Spring	Neap, Spring	Neap, Spring
Landform background	Delta front off the NB	Delta front off the NC	Delta front off the NC	Subtidal slope between NB and NC	Tidal flat between NB and NC	Tidal flat between SP and HB	Tidal flat in north HB

Table 2. Descriptions of the *in situ* observations at the seven sites. A, B, C, D, E, F and G represent the comprehensive observation sites in Fig. 1b. NB: North Branch. NC: North Channel. NP: North Passage. SP: South Passage. HB: Hangzhou Bay. *Based on hourly wind speed series from the European Centre for Medium-Range Weather Forecasts (ECMWF) (http://www.ecmwf.int/). The area behind the oblique line indicates a storm event.

the water content in the Yangtze subaqueous delta averaged 53%. The spatial pattern of the water content was opposite to that of the grain size (Fig. 4b).

The τ_{cr} values of the delta's surficial sediments ranged from 0.08 to 0.23 N/m² with an average of 0.13 N/m², which was overall slightly higher than that in the Yangtze subaqueous delta (0.11 N/m²) and much lower than that of the Pleistocene relic sands (0.18 N/m²) (Fig. 4c). The period when $\tau_{cw} > \tau_{cr}$ comprised 21–79% (48 ± 24%) of the observations during neap tides and 58–91% (78 ± 10%) of the observations during spring tides under normal winds at the observation sites. At a shallow site, τ_{cw} was always significantly larger than τ_{cr} during peak storm events, and the period when $\tau_{cw} > \tau_{cr}$ comprised 100% of the observations (Table 1 and Fig. 3).

The vertical trend in the τ_{cr} of the sediment cores in the upper most several metres was generally non-significant, although a slight trend of increase with depth was found in a few cores (Fig. 5). Based on the hydrodynamic measurements, the τ_{cr} for the upper most several metres was much higher than τ_{cw-min} and much lower than $\tau_{cw-mean}$ and τ_{cw-max} (Fig. 5). Based on CHIRP subbottom seismic profiling measurements, the sediments deposited during the past 2000 years is approximately 10–20 m in thickness (Fig. 6). These modern sediments are fine grained and have a similar median size to the surficial sediments.

Discussion

A comparison between the τ_{cw} and τ_{cr} values at the observation sites suggests that the Yangtze subaqueous delta was widely erodible during most of the study period. The seabed at the observation sites with water depths from <1 m to 21 m (Fig. 1b and Table 2) was not erodible only during slack waters under calm weather, which generally
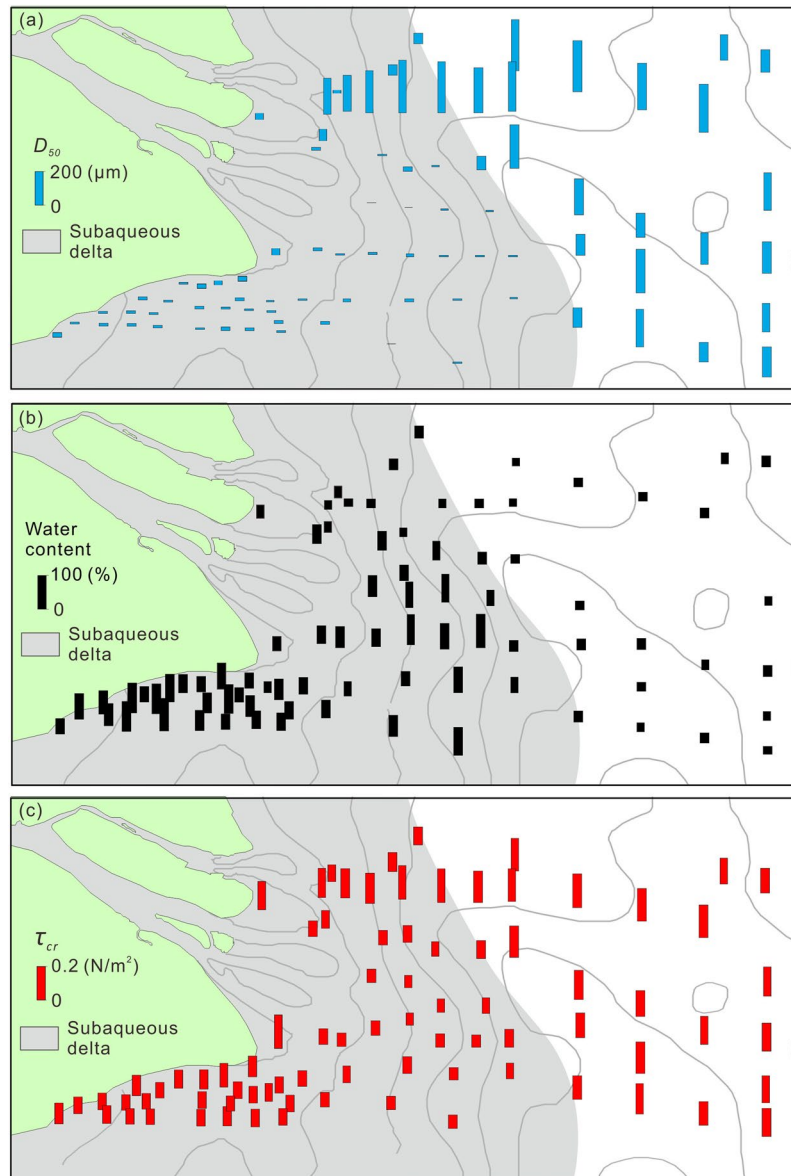
Figure 4. Histograms of the median size (D_{50}, in blue) (**a**), water content (in black) (**b**) and the τ_{cr} of the surficial sediments (in red) (**c**). The figures were created using ArcGIS 10.1 (www.esri.com/software/arcgis) and CorelDRAW Graphics Suite X6 (http://www.coreldraw.com/en/product/graphic-design-software).

comprised less than 40% of the study period (Table 1). It can be inferred that the erodibility in the subaqueous delta deeper than 21 m is comparable to the erodibility at the observation sites due to the similarity of tidal conditions[28] and comparable τ_{cr} values (Fig. 4c). The lack of a significant vertical trend in the τ_{cr} values of the core sediments suggests that the deposit layers are relatively homogenous for the upmost approximately 20 metres. This vertical stability does not reflect the seasonal changes in the erodibility of the real-time surficial sediment. According to the present Yangtze's sediment discharge (ca. 120 Mt/yr), its seasonal variability, and the subaqueous delta area (>10, 000 km^2), the deposition in the subaqueous delta during summer can be several centimetres in thickness. The erodibility of this fresh deposition must be even lower than that shown above (the upper 30 cm of the sediment sampled during the dry season). This low erodibility was also verified using known erosion dynamics produced by other researchers. For example, vertical degradation appeared in the mouth area of the North Branch (Fig. 1b) between 1997 and 2012 with a mean rate of −6.7 cm/yr and margin recession was also noted in the subaqueous delta front offshore of the South Branch[25]. Du et al.[24] also reported an erosion rate of approximately 2 cm/yr at the mouth area off the South Branch. The amount of sediment eroded from the subaqueous delta was more than 1 billion tons from 2002 to 2013 and mainly occurred between −6.4 m and −19 m isobaths[29]. In contrast, high and dense vegetation in the salt marshes of the Yangtze Delta efficiently attenuates waves and currents[30, 31], and the τ_{cw} is generally lower than the τ_{cr} of the bed sediments[32], which suggest a much lower erodibility. However, marsh edge collapses can result in the loss of salt marshes[33, 34]. Tidal flat erosion is expected to create steep slope along the lower marsh edge, and marsh edge collapses subsequently shrinks salt marshes.
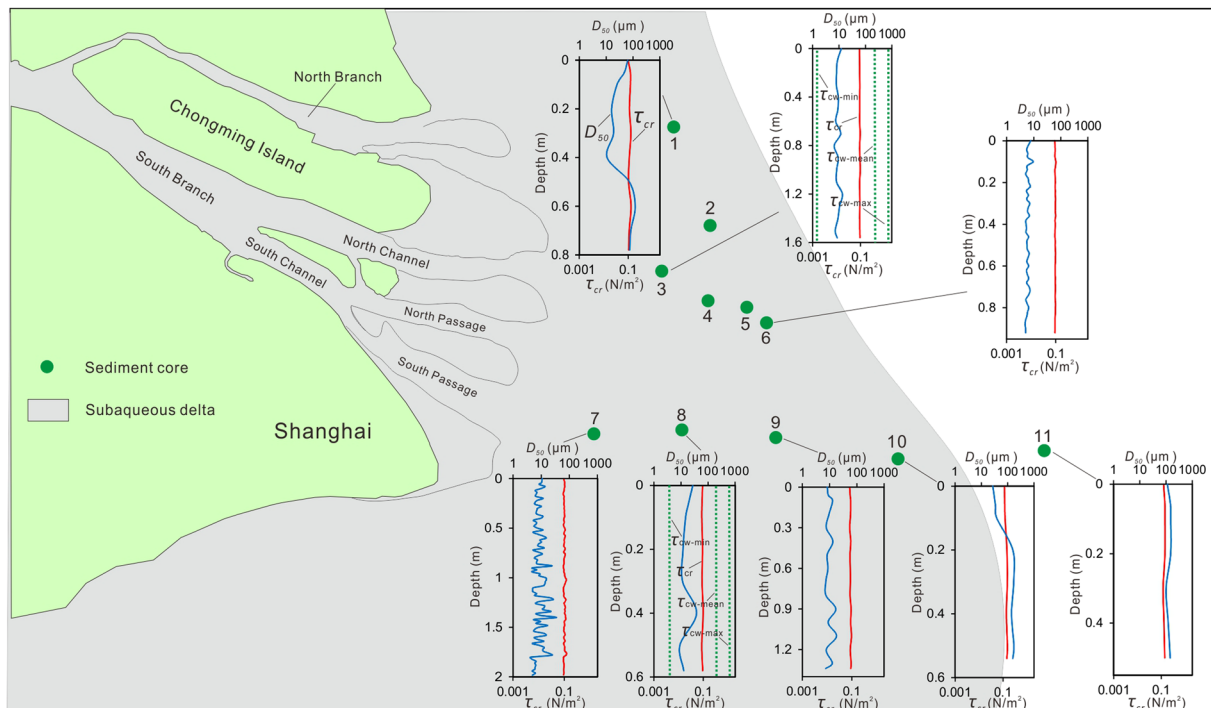
Figure 5. Vertical changes of the D_{50} (in blue) and τ_{cr} of the sediment cores (in red), and the measured characteristic τ_{cw} values (in green) compared to τ_{cr} values at the observation sites ($\tau_{cw\text{-min}}$, $\tau_{cw\text{-mean}}$ and $\tau_{cw\text{-max}}$ represent the minimal, mean and maximum τ_{cw} values, respectively). The figures were created using ArcGIS 10.1 (www.esri.com/software/arcgis) and CorelDRAW Graphics Suite X6 (http://www.coreldraw.com/en/product/graphic-design-software).
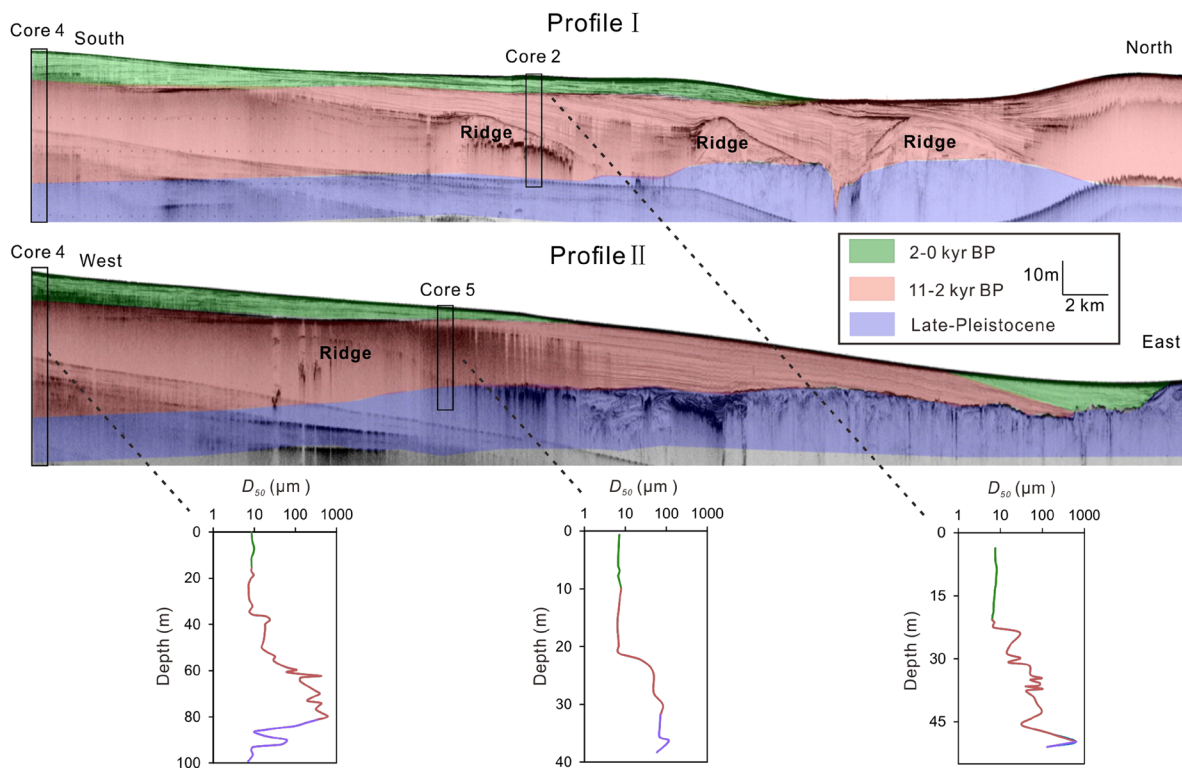

Figure 6. Two CHIRP seismic profiles and three cores in the Yangtze delta (modified from *Xu et al.*[57]). Three units are coloured by green, red and blue from top to bottom. The vertical variations in core sediment grain size are also shown in different colours. BP = Before Present, where present is 1950 A.D.

An erodible seabed does not necessarily lead to net erosion. Both erosion and deposition events occur during a tidal cycle. Net seabed erosion/accretion depends on the balance between the erosion flux and deposition flux[35–37]. The erosion flux is determined by the sediment erodibility, whereas the deposition flux is determined by the suspended sediment concentration[38, 39]. Thus, net erosion of the Yangtze Delta can be expected under sediment starvation, given the erodible seabed. Longshore currents play an important role in residual sediment transport. The suspended sediment concentrations in the Yangtze Estuary and adjacent coastal waters has significantly reduced in response to the decrease in riverine sediment discharge[40, 41], which would decrease the deposition flux and may result in net erosion through or within the subaqueous delta. In fact, a few of the most recent studies support this finding[24, 25]. Of course, the morphological response to a decline in the riverine sediment discharge may spatially vary, and accretion may continue somewhere in the large subaqueous delta[22]. Over the next several decades, the sediment discharge from the Yangtze River will further decrease as many new dams are constructed in the Yangtze basin[27], and continued delta erosion can be expected, particularly in the subaqueous delta front, where longshore currents develop. The CHIRP subbottom seismic profiles and vertical distribution of grain size (Fig. 6) suggest that τ_{cr} is low and the strata are most likely erodible for the uppermost 10-20 m of the subaqueous delta deposit. The erosion rate of the Yangtze subaqueous delta was 3–7 cm/yr over the past one to two decades[21, 24, 25]. Assuming that the delta experiences a similar erosion rate under decreased river sediment supply, increased coastal hydrodynamics and a slight downward increase in τ_{cr}, the erosion of the uppermost 10–20 m sediments will likely continue for the next decades of this century or even a few centuries.

Presumably, the erodibility and morphological trends of the world's deltas under river damming can differ greatly because the major influencing factors, namely the delta sediment properties, the local hydrodynamics for sediment resuspension, and the presence of longshore currents for the residual transport of sediment, can greatly change. The Yangtze Delta can likely be described as having a low τ_{cr}, high τ_{cw} and relatively strong longshore currents. Prior to river damming, the Yangtze Delta experienced rapid accretion due to the abundant fine-grained sediment supply[21, 42]. In other words, the uppermost several metres of sediment layers were not very compacted. The Yangtze Delta is under the impact of meso-macro tides and is exposed to the sizeable East China Sea, which suggests a high τ_{cw}. The monsoon-driven longshore currents off the Yangtze River mouth are relatively strong, with residual flow velocities that reach approximately 30 cm/s[43]. In comparison, the Mississippi and Nile deltas are under the impact of micro tides[44, 45]. However, perhaps many of the deltas would experience erosion under dam-generated sediment starvation, although deltas differ in terms of their erodibility. For example, the Mississippi subaqueous delta experienced severe erosion during storms[46]. Long-term coastal recession that was associated with river damming and wave-induced longshore currents was found in the Nile delta[6, 47].

Last but not least, increasing trends of longshore currents and wind waves are expected because global warming and sea surface wind speed increase have been extensively reported[10, 11, 13] and because of the results presented in Fig. 2. For example, *Gulev and Grigorieva*[12] reported positive trends of significant wave height over the North Pacific with a maximum of 8–10 cm/decade in the northeast Pacific. In addition, increasing water depth due to sea level rise[48, 49] can also result in increased wave height in the intertidal zone[50].

Conclusions

The upper several metres of fine-grained deposit in the Yangtze's subaqueous delta is overall high in water content, which leads to low τ_{cr} across wide areas. This delta is under the influence of meso to macro tides and exposed to the open sea, resulting in a high τ_{cw}. The seabed of this delta tends to be erodible during peak tidal flow phases but non-erodible during slack water phases. Under fair weather conditions, the erodible period comprises nearly 50% of the duration during neap tides and nearly 80% of the duration during spring tides. During storm events, the shallow seabed can always be erodible. Dam-induced sediment starvation reduces the deposition flux during non-erodible periods. Thus, the erosion flux may exceed the deposition flux within the tidal cycle. Net delta erosion can be seen together with strong longshore currents, which can transport sediment southward. Over the next several decades, continuous erosion can be expected for the uppermost several metres of sediments in the subaqueous delta, considering that the Yangtze sediment discharge will further decrease due to the construction of new dams and that the energy of tides and waves in coastal ocean will likely continue to increase under global warming and sea level rise. Delta erosion will threaten ecosystems and engineering facilities (e.g., shallowly buried oil, gas pipelines, optical cables and seawalls). Subaqueous deltaic erosion and the processes controlling sediment erodibility need to be one of the key topics of studies on global coastal protection and restoration.

Study area

The Yangtze River and its delta.   The Yangtze River originates on the Qinghai–Tibet Plateau and flows 6,300 km eastward to the East China Sea (Fig. 1a). Approximately 6,000 years BP, when the post-glacial sea level was near its maximum height, the mouth of the Yangtze River was approximately 300 km inland relative to the present coastline. Since then, the delta advanced due to the deposition of riverine sediments[51]. Over the past 2,000 years, the delta's progradation has accelerated due to catchment deforestation[26, 52]. However, coastal progradation has significantly slowed during the most recent decades because of the dam-generated decline in the Yangtze's sediment discharge[53, 54].

The current Yangtze mouth includes four outlets (Fig. 1b). Prior to the 18th century, the North Branch was the main outlet of the Yangtze's water and sediment discharge. During the 18th century, however, the major river flow shifted to the South Branch[52]. Now, more than 95% of the Yangtze's water and sediment flows into the sea via the three outlets of the South Branch[55]. The fine sediments from the Yangtze River formed a modern subaqueous delta off the Yangtze Estuary. Further seaward, this area is covered by Pleistocene relic sands[25], which were probably winnowed by the currents as the sea level rose since the Last Glacial Maximum. Coarse sands due to severe erosion between 1997 and 2012 were also found in the mouth area of the North Branch[25] (Fig. 1b). The Yangtze Estuary and adjacent waters are meso-macro tidal and influenced by monsoons. The wind speeds are highly

variable, with multi-year averages of 4–5 m/s and a maximum of 36 m/s[32]. During winter, a strong southward longshore current system develops under the influence of northerly monsoon winds (Fig. 1a), transporting a bulk of sediment away from the Yangtze Delta. The deposition of this sediment has formed a Holocene mud wedge that is several hundred kilometres long in the inner continental shelf of the East China Sea[56, 57].

Methods

Datasets. The Yangtze River's water and sediment discharges were obtained from the Yangtze Water Resources Committee (YWRC), Ministry of Water Resource of China. The data on wind speed and significant wave height at Sheshan Station (Fig. 1b) were downloaded from the European Centre for Medium-Range Weather Forecasts (ECMWF) (http://www.ecmwf.int/). The global sea level data were downloaded from the sea level group of the Commonwealth Scientific and Industrial Research Organization (CSIRO), Australia's national science agency (http://www.cmar.csiro.au/); these data was updated from *Church and White*[48]. The mean coastal sea level data for China were derived from the State Oceanic Administration, People's Republic of China (http://www.soa.gov.cn/).

The top sediment (the uppermost 30 cm) and core sediments were sampled in March 2012 and January–March 2013 using a box sampler and a gravity corer, respectively. Two high-resolution seismic profiles were collected after 2003 using a CHIRP sonar sub-bottom profiler (EdgeTech 0512i), and more details can be found in *Xu et al.*[57] (Fig. 6). One 600-kHz Acoustic Doppler Current Profiler (ADCP, four flow sensors with a 0.5 m bin size, 0.25 m blanking distance, Teledyne RD Instruments, Inc., California, USA) was used to measure the current velocity profile at sites A, B, C and D (Fig. 1b; Table 2). Another ADCP (1.0 MHz high-resolution profiler, Nortek AS, Norway), placed at 70 cm above the sediment surface and looking downward, was utilized to measure the current velocity profiles on the tidal flats at sites E, F and G (Fig. 1b; Table 2). The blanking distance was 40 cm, and the cell size was set to 2.5 cm. Each velocity profile was collected at a frequency of 1 Hz over a duration of 60 seconds during a burst interval of 5 minutes. The current velocity profile at an interval of 10 seconds continually lasted for at least 26 hours (more than 2 tidal cycles) at each site during both spring and neap tides. An SBE-26plus Seagauge (Sea-Bird Electronics, Washington, USA) was utilized to measure wave heights, wave periods, and water depths, etc., using a self-logging sensor. The sampling rate was set to 4 Hz over a duration of 256 seconds during each burst of 10 minutes. The sediment grain size was analysed in the laboratory using a Laser Diffraction Particle Size Analyser, Beckman-Coulter Ls100Q (Beckman Coulter Inc., California, USA). The water content was defined as the ratio of the water weight to the dry sediment weight.

Calculation of τ_{cr} and τ_{cw}. In terms of τ_{cr} (critical bed shear stress for erosion), when sediments on the seabed are mainly non-cohesive deposits, *van Rijn*'s[58] equation is acceptable in coastal and estuarine areas. *Taki*[59] produced another formula that is widely used for cohesive fine sediments. Although *Zhang*[60] found that a value of 50 μm for sediments that contain water was the critical value to distinguish cohesive sediments from non-cohesive sediments, a comparison of the two methods that are used to calculate τ_{cr} was still conducted. When the sediments were finer than 50 μm, the results from *van Rijn*[58] were apparently smaller, which did not match practical situations.

When the sediment was finer than 50 μm, τ_{cr} was calculated as follows[59]:

$$\tau_{cr} = 0.05 + \beta \left\{ \frac{1}{[(\pi/6)(1 + sW)]^{1/3} - 1} \right\}^2 \tag{1}$$

where $\beta = 0.3$ (for relatively high water content), w is the water content, $s = (\rho_s/\rho_w) - 1$, ρ_s is sediment particle density, and ρ_w is seawater density.

When the sediment was coarser than 50 μm, τ_{cr} was calculated as follows[58]:

$$\tau_{cr} = \theta_{cr}(\rho_s - \rho_w)g\mathrm{d}_{50} \tag{2}$$

in which the critical Shields parameter[61]: $\theta_{cr} = 0.11 D_*^{-0.54}$, the dimensionless particle size $D* = \left[\frac{s - 1g}{V^2}\right]^{\frac{1}{3}} \mathrm{d}_{50}$, $s = \rho_s/\rho_w$, θ_{cr} is the dimensionless Shields value, and g is the acceleration of gravity.

τ_c (current shear stress, N/m²) was calculated using the following equation[62]:

$$\tau_c = \rho_w u*_c^2 \tag{3}$$

where ρ_w is the seawater density (measured to be 1030 kg/m³) and $u*_c$ (bed friction velocity, m/s) was derived from linear regression (P < 0.05) based on the logarithmic distribution of vertical current velocity profiles according to the equation between $u_c(z)$ and $\ln z$[63]:

$$u_c(\mathrm{z}) = \frac{u*_c}{\kappa} \ln z - \frac{u*_c}{\kappa} \ln z_0 \tag{4}$$

in which z is the height of the velocity profile above the bed (m), z_0 is the bed roughness length (m), $u_c(z)$ is the current speed at z (m/s), and κ is Von Karman's constant (0.4).

τ_w (wave shear stress, N/m²) can be calculated as[58]:

$$\tau_w = \frac{1}{4}\rho_w f_w \hat{U}^2_\delta \tag{5}$$

where f_w is the friction coefficient which is determined by the hydraulic regime:

$$f_w = \begin{cases} 2\mathrm{Re}_w^{-0.5}, & \mathrm{Re}_w \leq 10^5 \text{ (laminar)} \\ 0.0521\mathrm{Re}_w^{-0.187}, & \mathrm{Re}_w > 10^5 \text{ (smooth turbulent)} \\ 0.237r^{-0.52}, & \text{(rough turbulent)} \end{cases} \tag{6}$$

in which the wave Reynolds number: $\mathrm{Re}_w = \frac{\hat{U}_\delta \hat{A}_\delta}{\nu}$, the relative roughness: $r = \frac{\hat{A}_\delta}{k_s}$, the Nikuradse roughness: $k_s = 2.5D_{50}$, D_{50} is the median grain size of the bed sediment, and ν is the kinematic viscosity of sea water (m²/s).

The peak orbital excursion ($\hat{A}_\delta$) and peak orbital velocity ($\hat{U}_\delta$) can be expressed as:

$$\hat{A}_\delta = \frac{H}{2\,\sinh(kh)} \tag{7}$$

$$\hat{U}_\delta = \omega\hat{A}_\delta = \frac{\pi H}{T\,\sinh(kh)} \tag{8}$$

in which H is the wave height (m), the wave number (m⁻¹) k = 2π/L, the wave length (m) $L = (gT^2/2\pi)\tanh(kh)$, h is the water depth (m), ω is the angular velocity (s⁻¹), and T is the wave period (s).

τ_{cw} (combined current-wave shear stress, N/m²) was calculated by ref. 64:

$$\tau_{cw} = \tau_c\left[1 + 1.2\left(\frac{\tau_w}{\tau_c + \tau_w}\right)^{3.2}\right] \tag{9}$$

These models are widely employed to calculate τ_{cr} and τ_{cw}[32, 39, 65–67].

References

1. Blum, M. D. & Roberts, H. H. Drowning of the Mississippi Delta due to insufficient sediment supply and global sea-level rise. *Nat. Geosci.* **2**, 488–491 (2009).
2. Giosan, L., Syvitski, J., Constantinescu, S. & Day, J. Climate Change: protect the world's deltas. *Nature* **516**, 31–33 (2014).
3. Tessler, Z. D. *et al.* Profiling risk and sustainability in coastal deltas of the world. *Science* **349**, 638–643 (2015).
4. Vörösmarty, C. J. *et al.* Anthropogenic sediment retention: major global impact from registered river impoundments. *Global planet. change* **39**, 169–190 (2003).
5. Walling, D. E. Human impact on land–ocean sediment transfer by the world's rivers. *Geomorphology* **79**, 192–216 (2006).
6. Milliman, J. D. & Farnsworth, K. L. *River discharge to the coastal ocean: A global synthesis.* Cambridge University Press, Cambridge (2011).
7. Syvitski, J. P. M., Vörösmarty, C. J., Kettner, A. J. & Green, P. Impact of humans on the flux of terrestrial sediment to the global coastal ocean. *Science* **308**, 376–380 (2005).
8. Meade, R. H. & Moody, J. A. Causes for the decline of suspended–sediment discharge in the Mississippi River system, 1940–2007. *Hydrol. Process.* **24**, 35–49 (2010).
9. Wang, H. *et al.* Recent changes of sediment flux to the western Pacific Ocean from major rivers in East and Southeast Asia. *Earth-Sci. Rev.* **108**, 80–100 (2011).
10. Trenberth, K. E. *et al.* Global warming and changes in drought. *Nat. Clim. Change* **4**, 17–22 (2014).
11. Wallace, J. M., Held, I. M., Thompson, D. W., Trenberth, K. E. & Walsh, J. E. Global warming and winter weather. *Science* **343**, 729–730 (2014).
12. Gulev, S. K. & Grigorieva, V. Last century changes in ocean wind wave height from global visual wave data. *Geophys. Res. Lett.* **31**, doi:10.1029/2004GL021040 (2004).
13. Liu, Z. *et al.* Long-term trend and special Characteristics of sea surface wind speed in the Northwest Pacific Ocean during the last 22 years. *Ocean Technol.* **30**, 127–130 (2011).
14. Fanos, A. M. The impacts of human activities on the erosion and accretion of the Nile Delta coast. *J. Coastal Res.* **11**, 821–833 (1995).
15. Sánchez-Arcilla, A., Jiménez, J. A. & Valdemoro, H. I. The Ebro Delta: Morphodynamics and vulnerability. *J. Coastal Res.* **14**, 754–772 (1998).
16. Ly, C. K. The role of the Akosombo Dam on the Volta River in causing coastal erosion in central and eastern Ghana. *Mar. Geol.* **37**, 323–332 (1999).
17. Carriquiry, J. D., Sánchez, A. & Camacho-Ibar, V. F. Sedimentation in the northern Gulf of California after cessation of the Colorado River discharge. *Sediment. Geol.* **144**, 37–62 (2001).
18. Chu, Z. X., Sun, X. G., Zhai, S. K. & Xu, K. H. Changing pattern of accretion/erosion of the modern Yellow River (Huanghe) subaerial delta, China: based on remote sensing images. *Mar. Geol.* **227**, 13–30 (2006).
19. Yang, S. L., Xu, K. H., Milliman, J. D., Yang, H. F. & Wu, C. S. Decline of Yangtze River water and sediment discharge: Impact from natural and anthropogenic changes. *Sci. Rep.* **5**, doi:10.1038/srep12581 (2015).
20. Nilsson, C., Reidy, C. A., Dynesius, M. & Revenga, C. Fragmentation and flow regulation of the world's large river systems. *Science* **308**, 405–408 (2005).
21. Yang, S. L., Milliman, J. D., Li, P. & Xu, K. H. 50,000 dams later: Erosion of the Yangtze River and its delta. *Global Planet. Change* **75**, 14–20 (2011).
22. Dai, Z. J., Liu, J. T., Wei, W. & Chen, J. Y. Detection of the Three Gorges Dam influence on the Changjiang (Yangtze River) submerged delta. *Sci. Rep.* **4**, 6600, doi:10.1038/srep06600 (2014).
23. Luan, H. L., Ding, P. X., Wang, Z. B., Ge, J. Z. & Yang, S. L. Decadal morphological evolution of the Yangtze Estuary in response to river input changes and estuarine engineering projects. *Geomorphology* **265**, 12–23 (2016).
24. Du, J. L., Yang, S. L. & Feng, H. Recent human impacts on the morphological evolution of the Yangtze River delta foreland: A review and new perspectives. *Estuar. Coast. Shelf. S.* **181**, 160–169 (2016).
25. Luo, X. X., Yang, S. L. Wang, R. S., Zhang, C. Y. & Li, P. New evidence of the Yangtze delta recession after closing of the Three Gorges Dam. *Sci. Rep.* **7**, doi:10.1038/srep41735 (2017).
26. Yang, S. L., Ding, P. X. & Chen, S. L. Changes in progradation rate of the tidal flats at the mouth of the Changjiang River, China. *Geomorphology* **38**, 167–180 (2001).

27. Liu, J., Yang, S. L., Zhu, Q. & Zhang, J. Controls on suspended sediment concentration profiles in the shallow and turbid Yangtze Estuary. *Cont. Shelf Res.* **90**, 96–108 (2014).
28. Wu, H., Zhu, J., Shen, J. & Wang, H. Tidal modulation on the Changjiang River plume in summer. *J. Geophys. Res.* **116**, doi:10.1029/2011JC007209 (2011).
29. Li, B., Yan, X., He, Z., Chen, Y. & Zhang, J. Impacts of the Three Gorges Dam on the bathymetric evolution of the Yangtze River Estuary. *Chinese Science Bulletin* **60**, 1735–1744 (2015).
30. Yang, S. L. The role of scirpus marsh in attenuation of hydrodynamics and retention of fine sediment in the Yangtze estuary. *Estuar. Coast Shelf S.* **47**, 227–233 (1998).
31. Yang, S. L., Shi, B. W., Bouma, T. J., Ysebaert, T. & Luo, X. X. Wave attenuation at a salt marsh margin: a case study of an exposed coast on the Yangtze Estuary. *Estuar. Coast.* **35**, 169–182 (2012).
32. Shi, B. W., Yang, S. L. & Wang, Y. P. Intertidal erosion and deposition interpreted from field observations of hydrodynamic and sedimentary processes: A case study from an exposed, meso–macrotidal and highly turbid mudflat–saltmarsh transition. *Cont. Shelf Res.* **90**, 109–116 (2014).
33. van de Koppel, J., van der Wal, D., Bakker, J. P. & Herman, P. M. J. Self-organization and vegetation collapse in salt marsh ecosystems. *Am. Nat.* **165**, 1–12 (2005).
34. van de Plassche, O. *et al.* Salt-marsh erosion associated with hurricane landfall in southern New England in the fifteenth and seventeenth centuries. *Geology* **34**, 829–832 (2006).
35. Jestin, H., Bassoullet, P., Le Hir, P., L'Yavanc, J. & Degres, Y. Development of ALTUS, a high frequency acoustic submersible recording altimeter to accurately monitor bed elevation and quantify deposition and erosion of sediments. *Oceans* **98**, 189–194 (1998).
36. Lumborg, U. Modelling the deposition, erosion, and flux of cohesive sediment through Øresund. *J. Mar. Syst.* **56**, 179–193 (2005).
37. Maan, D. C., Prooijen, B. C., Wang, Z. B. & De Vriend, H. J. Do intertidal flats ever reach equilibrium? *J. Geophys. Res.* **120**, 2406–2436 (2015).
38. Winterwerp, J. C. & Van Kesteren, W. G. Introduction to the physics of cohesive sediment dynamics in the marine environment. Elsevier, Amsterdam (2004).
39. Zhu, Q., van Prooijen, B. C., Wang, Z. B., Ma, Y. X. & Yang, S. L. Bed shear stress estimation on an open intertidal flat using *in situ* measurements. *Estuar. Coast. Shelf S.* **182**, 190–201 (2016).
40. Li, P. *et al.* Spatial, Temporal, and Human-Induced Variations in Suspended Sediment Concentration in the Surface Waters of the Yangtze Estuary and Adjacent Coastal Areas. *Estuar. Coast.* **35**, 1316–1327 (2012).
41. Yang, S. L. *et al.* Downstream sedimentary and geomorphic impacts of the Three Gorges Dam on the Yangtze River. *Earth–Sci. Rev.* **138**, 469–486 (2014).
42. Liu, M. & Fan, D. Geochemical records in the subaqueous Yangtze River delta and their responses to human activities in the past 60 years. *Chinese Sci. Bull.* **56**, 552–561 (2011).
43. Hu, H., Li, S. D., Pan, D. A. & Gu, G. C. Analysis of the residual current characteristics in the Changjiang River estuary area. *Dynamic process and geomorphological evolution in the Changjiang River estuary area* (in Chinese). Shanghai Science and Technology Press, Shanghai, China (1988).
44. Stanley, D. J. & Warne, A. G. Nile Delta in its destruction phase. *J. Coastal Res.* **14**, 795–825 (1998).
45. Törnqvist, T. E., Bick, S. J., van der Borg, K. & de Jong, A. F. How stable is the Mississippi Delta? *Geology* **34**, 697–700 (2006).
46. Turner, R. E., Baustian, J. J., Swenson, E. M. & Spicer, J. S. Wetland sedimentation from hurricanes Katrina and Rita. *Science* **314**, 449–452 (2006).
47. Albert, P. & Jorge, G. Coastal changes in the Ebro delta: Natural and human factors. *J. Coast. Conserv.* **4**, 17–26 (1998).
48. Church, J. A. & White, N. J. Sea-level rise from the late 19th to the early 21st century. *Surv. Geophys.* **32**, 585–602 (2011).
49. Rignot, E., Velicogna, I., Van den Broeke, M. R., Monaghan, A. & Lenaerts, J. T. M. Acceleration of the contribution of the Greenland and Antarctic ice sheets to sea level rise. *Geophys. Res. Lett.* **38**, doi:10.1029/2011GL046583 (2011).
50. Storlazzi, C. D., Elias, E., Field, M. E. & Presto, M. K. Numerical modeling of the impact of sea-level rise on fringing coral reef hydrodynamics and sediment transport. *Coral Reefs* **30**, 83–96 (2011).
51. Hori, K. *et al.* Sedimentary facies and Holocene progradation rates of the Changjiang (Yangtze) delta, China. *Geomorphology* **41**, 233–248 (2001).
52. Chen, J. Y., Zhu, H. F., Dong, Y. F. & Sun, Y. M. Development of the Changjiang estuary and its submerged delta. *Cont. Shelf Res.* **4**, 47–56 (1985).
53. Yang, S. L. *et al.* Delta response to decline in sediment supply from the Yangtze River: evidence of the recent four decades and expectations for the next half-century. *Estuar., Coast. Shelf S.* **57**, 589–599 (2003).
54. Yang, S. L. *et al.* Impact of Dams on Yangtze River Sediment Supply to the Sea and Delta Wetland Response. *J. Geophys. Res.* **110**, doi:10.1029/2004JF000271 (2005).
55. Dai, Z., Fagherazzi, S., Mei, X., Chen, J. & Meng, Y. Linking the infilling of the North Branch in the Changjiang (Yangtze) estuary to anthropogenic activities from 1958 to 2013. *Mar. Geol.* **379**, 1–12 (2016).
56. Milliman, J. D., Shen, H. T., Yang, Z. S. & Meade, R. H. Transport and deposition of river sediment in the Changjiang estuary and adjacent continental shelf. *Cont. Shelf Res.* **4**, 37–45 (1985).
57. Xu, K. H. *et al.* Provenance, structure, and formation of the mud wedge along inner continental shelf of the East China Sea: a synthesis of the Yangtze dispersal system. *Mar. Geol.* **291**, 176–191 (2012).
58. van Rijn, L. C. *Principles of sediment transport in rivers, estuaries and coastal seas*. Aqua Publication Amsterdam, the Netherlands (1993).
59. Taki, K. Critical shear stress for cohesive sediment transport. *Proceedings in Marine Science* **3**, 53–61 (2001).
60. Zhang, R. J. *Dynamics of river sediment transport*. China Water Power Press, Beijing (1989).
61. Miller, M. C., McCave, I. N. & Komar, P. Threshold of sediment motion under unidirectional currents. *Sedimentology* **24**, 507–527 (1977).
62. Whitehouse, R. J. S., Soulsby, R., Roberts, W. & Mitchener, H. J. *Dynamics of Estuarine Muds—A Manual for Practical Applications*. Thomas Telford, London (2000).
63. Kapdasli, M. S. & Dyer, K. R. Threshold conditions for sand movement on a rippled bed. *Geo-mar. let.* **6**, 161–164 (1986).
64. Soulsby, R. L. Bed shear-stresses under combined waves and currents on smooth and rough beds. *Report TR137*, HR Wallingford (2005).
65. Andersen, T. J., Fredsoe, J. & Pejrup, M. *In situ* estimation of erosion and deposition thresholds by Acoustic Doppler Velocimeter (ADV). *Estuar. Coast. Shelf S.* **75**, 327–336 (2007).
66. Salehi, M. & Strom, K. Measurement of critical shear stress for mud mixtures in the San Jacinto estuary under different wave and current combinations. *Cont. Shelf Res.* **47**, 78–92 (2012).
67. Green, M. O. & Coco, G. Review of wave-driven sediment resuspension and transport in estuaries. *Rev. Geophys.* **52**, 77–117 (2014).

Acknowledgements

Author Contributions

S.L. Yang conceived the study. H.F. Yang, H. Wu, B.W. Shi, Q. Zhu and W.X. Zhang conducted the field observation, data analyses and calculations. H.F. Yang wrote the draft of the manuscript and prepared the figures. S.L. Yang, K.H. Xu and Z.S. Yang contributed to the improvement of the manuscript. All authors reviewed the manuscript.

Additional Information

Supplementary information accompanies this paper at doi:10.1038/s41598-017-10958-y

Competing Interests: The authors declare that they have no competing interests.

Publisher's note: Springer Nature remains neutral with regard to jurisdictional claims in published maps and institutional affiliations.